Chaos
An Interdisciplinary Journal of Nonlinear Science

RESEARCH ARTICLE | JUNE 05 2025

Chaos, dynamic trapping, and transport of swimming microbes in a vortex chain flow

Nghia Le ; Thomas H. Solomon

Chaos 35, 063116 (2025)
https://doi.org/10.1063/5.0270869
CHORUS

Chaos, dynamic trapping, and transport of swimming microbes in a vortex chain flow

Cite as: Chaos 35, 063116 (2025); doi: 10.1063/5.0270869
Submitted: 13 March 2025 · Accepted: 12 May 2025 ·
Published Online: 5 June 2025

Nghia Le and Thomas H. Solomon[a)]

AFFILIATIONS

Department of Physics and Astronomy, Bucknell University, Lewisburg, Pennsylvania 17837, USA

[a)]**Author to whom correspondence should be addressed:** tsolomon@bucknell.edu.

ABSTRACT

We present experiments on chaotic motion of self-propelled (active) particles in a time-independent, two-dimensional vortex chain flow. We track *Tetraselmis* microbes and calculate the variance of a spreading distribution of these microbes in the flow. For small non-dimensional swimming speed v_0, we find subdiffusion with variance $\langle x^2 \rangle \sim t^\gamma$ with $\gamma < 1$; transport is diffusive ($\gamma = 1$) for larger v_0. Subdiffusion for small v_0 is due to dynamic trapping of microbes to islands of ordered trajectories surrounded by a sea of chaotic motion; these islands disappear for larger v_0. We calculate *Lagrangian-averaged trajectories* (LATs) from the experimental data and use the LATs to measure trapping time probability distributions $P(t)$. We find regimes with $P(t) \sim t^{-\nu}$ with $\nu < 2$ for small v_0, consistent with the measured subdiffusion.

Fluid flows affect the motion of active, self-propelled particles in a wide range of systems from bacteria swimming within blood flows to fish and boats moving in the oceans. Idealized numerical models demonstrate that the motion of active particles in a flow can be chaotic, even for smooth, laminar fluid flows. In real systems, however, swimming noise and flow complexities often obscure signatures of deterministic chaos. We study the motion of swimming microbes (*Tetraselmis*) in a vortex chain flow. We find a regime of sub-diffusion ($\langle x^2(t) \rangle \sim t^\gamma$ with $\gamma < 1$) for microbes swimming with a small non-dimensional swimming speed v_0; we find normal (enhanced) diffusion ($\gamma = 1$) for larger v_0. The subdiffusive behavior is due to a hopping-and-trapping mechanism;[1] microbes undergoing chaotic trajectories in the flow are trapped dynamically to islands of ordered behavior that are predicted by simulations for small v_0. These islands disappear at larger v_0, consistent with measurements of normal diffusion for those swimming speeds. We calculate *Lagrangian-averaged trajectories* (LATs) from the experimental data and use these LATs to verify the dynamic trapping of the slow-swimming microbes and to measure trapping time probability distributions. These results demonstrate that deterministic chaos can have significant, measurable effects on the transport of active particles, even in the realistic case where there is noise in the swimming of those particles.

I. INTRODUCTION

The behavior of self-propelled (active) particles is often heavily influenced by the presence of fluid flows, a problem with significant applications for a wide range of systems including: the spread of diseases in a moving (flowing) population;[2,3] the ability of microbes to cause infections in human lungs,[4] guts,[5] and circulatory systems;[6] the dynamics of evolving ecosystems (including predator–prey systems and plankton blooms) in flowing bodies of water;[7–9] and the development of strategies for minimizing energy use for self-propelled devices in oceanic and atmospheric flows.[10] Fluid flows also affect the behavior of propagating reaction fronts,[11,12] which can be considered as active impurities. Previous studies of active impurities in flows have focused on the role of rheotaxis;[13–15] the effects of swimming organisms on *Lagrangian coherent structures*[16–19] that inhibit the mixing of passive impurities;[20–22] microbe density variations and depletion zones in channel flows;[23,24] and theoretical studies of trapping, clustering, alignment, and topology in vortex flow.[25–28] Recent experiments by our group have also demonstrated the existence of swimming invariant manifolds (SwIMs) and burning invariant manifolds that act as one-way barriers that block the motion of active particles in a flow.[11,29–31] Those studies also demonstrated[31] how these manifolds combine to form "chute" structures that transport microbes locally between different unit cells of the flow.

Long-range transport of active particles in the presence of fluid flows is a relatively unexplored problem. In the absence of fluid flows, long-range transport of active particles has been shown to be modeled well as enhanced diffusion (variance $\langle r^2 \rangle \sim t^\gamma$ with $\gamma = 1$) for free-swimming microbes[32] or *subdiffusion* ($\gamma < 1$) for swimming bacteria undergoing hopping-and-trapping in a confined porous medium.[1] Long-range transport is also strongly influenced by the possibility of chaotic advection of the impurities. It is well-known that *passive* (non-active) particles moving in laminar flows can undergo chaotic trajectories, even for very simple, well-ordered flows.[33–36] Numerical and theoretical studies have shown that chaotic motion is possible also for active particles in a flow,[37] even for two-dimensional, time-independent flows (for which passive mixing cannot be chaotic). There have been studies of the behavior of swimming microbes in time-dependent vortex flows where passive mixing is chaotic,[25,38,39] but there has been no previous experimental evidence of deterministic chaos for swimming particles themselves in laminar flows. Chaotic advection can also have significant effects on long-range transport behavior of impurities in a flow. In particular, *dynamic trapping*[40] of chaotic trajectories to islands of ordered behavior can result in anomalous diffusion where the growth of the variance of a distribution of particles is nonlinear in time.[41–43]

In this article, we present experimental evidence (supported by numerical simulations) of the effects of chaotic motion and dynamic trapping on the long-range transport of swimming microbes in a laminar, time-independent, two-dimensional vortex chain flow. We track the motion of individual swimming *Tetraselmis* microbes in the flow and determine the one-dimensional variance $\langle x^2(t) \rangle$ from these trajectories. We find that for small non-dimensional swimming speeds v_0, the long-range transport is sub-diffusive with $\gamma < 1$; the transport is diffusive ($\gamma = 1$) for larger swimming speeds. We show that the subdiffusion for small v_0 is due to dynamic trapping of microbes to ordered islands within a larger chaotic sea.

In Sec. II, we discuss the conditions for chaotic mixing, dynamic trapping, and the equations of motion for active particles moving in a fluid flow. In Sec. III, we describe the experimental techniques, including the mechanisms for generation of the vortex flow, details about the microbes and their handling, and data collection and analysis. In Sec. IV, we present results of numerical simulations that demonstrate the coexistence of chaotic and ordered motion of microbes in a vortex chain flow. We present the experimental results in Sec. V and discuss analysis of the experimental data with a Lagrangian-averaged framework in Sec. VI. We discuss our findings in Sec. VII.

II. BACKGROUND

A. Chaotic advection, transport barriers, and dynamic trapping

Chaotic particle motion[44,45] in laminar flows is possible if there are at least three phase space dimensions that describe the motion. For passive (non-swimming) particles, chaotic motion is possible in two-dimensional (2D), laminar flows, but only if the flow is time-dependent, with time t providing the third essential phase space dimension. As an example, chaotic advection has been well-established for a 2D, oscillating vortex chain flow

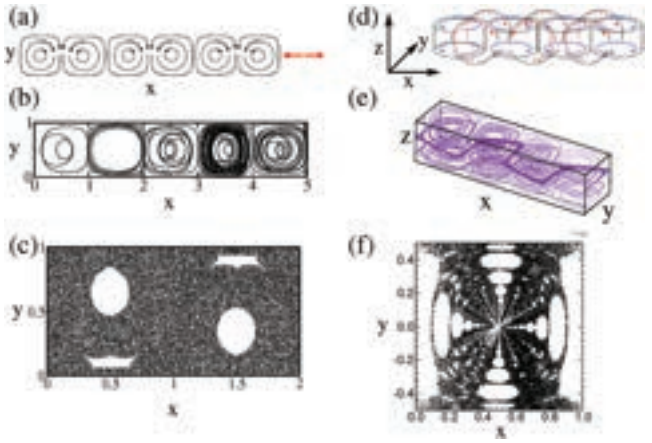

FIG. 1. Examples of chaotic mixing of passive impurities in laminar flows. In each image, distances are scaled by the vortex width. (a) Sketch of oscillating vortex chain flow. (b) Example of chaotic trajectory in the oscillating vortex chain flow. (c) Poincaré section showing locations of a single trajectory once every period of oscillation. (d) Sketch of paper-chain flow. (e) Example of chaotic trajectory in a time-independent, paper-chain flow. (f) Poincaré section showing the location of a single trajectory each time it crosses the midplane of the flow in the positive direction.

[Figs. 1(a)–1(c)].[34,46] If the flow is three-dimensional (3D), chaotic trajectories are possible even if the flow is time-independent.[47] An example is the 3D "paper-chain" flow [Figs. 1(d)–1(f)],[48] composed of the superposition of horizontal and vertical vortex chain flows, shifted by one-half of a vortex relative to each other.

Chaotic advection of tracers in a flow is characterized by complicated trajectories that are sensitive to initial conditions; two tracers that are located close to each other follow paths that diverge roughly exponentially in time from each other: $\Delta r(t) \sim \Delta r_0 e^{\lambda t}$ where Δr_0 is the initial separation (assumed small) between the tracers and λ is the largest Lyapunov exponent.

It is common for a flow to have both ordered and chaotic trajectories, depending on the location of the tracer in the flow. The coexistence of ordered and chaotic trajectories can be shown by plotting Poincaré sections, shown numerically in Figs. 1(c) and 1(f) for the oscillating vortex chain and paper-chain flows, respectively. For a 2D, time-periodic flow such as the oscillating vortex chain flow, a Poincaré section is determined by plotting the (x, y) location of a trajectory once every period of oscillation. For the 3D, time-independent, paper-chain flow, the Poincaré section is the plot of the (x, y) coordinate every time the trajectory crosses the $z = 0$ plane in the positive direction. In both Figs. 1(c) and 1(f), regions in the flow with ordered trajectories show up as white "islands" with no points in the Poincaré section.

Ordered islands exist because boundaries between ordered islands and the chaotic regions act as barriers called Kolmogorov–Arnold–Moser (KAM) invariant tori[35,45] across which tracers cannot pass. These barriers can lead to the trapping of particles inside the ordered regions. Also, *dynamic trapping*[40] is possible for tracers moving in a chaotic region; even though chaotic trajectories ideally never penetrate into ordered

regions, they can mimic ordered behaviors by sticking to the perimeters of the ordered regions with sticking time probabilities $P(t) \sim t^{-\nu}$. Dynamic trapping can be seen in Figs. 1(b) and 1(e) as heavier bands where the trajectory appears to almost repeat, e.g., the heavy band in the second-to-right vortex in Fig. 1(b) and the heavy band at the mid-height in Fig. 1(e).

Dynamic trapping of tracers in the chaotic regions of a flow can have a significant impact on long-range transport. In one-dimension (e.g., in the direction along a chain of vortices), transport is typically characterized by the variance $\langle x^2 \rangle \sim t^{\gamma}$. Localized sticking with power-law probability distribution functions (PDFs) is known to result in subdiffusion[43] with $\gamma = \nu - 1$ if the sticking exponent ν is in the range $1 < \nu < 2$. If $\nu > 2$, long-range transport is diffusive with $\gamma = 1$. Note that *superdiffusive* transport is possible with $\gamma > 1$ if there is dynamic trapping to islands that contain ordered trajectories that are unbounded. This mechanism has been used to explain Lévy flights and superdiffusive transport measured in laboratory experiments of passive transport in geophysical-motivated flows of co-rotating vortices sandwiched between jet regions.[42,49]

B. Active particles in fluid flows

For a self-propelled tracer, we consider a simplified spheroidal particle [Fig. 2(a)] with aspect ratio $\gamma = l_{||}/l_{\perp}$ and $\alpha = \frac{\gamma^2-1}{\gamma^2+1}$ swimming with a constant speed V_0. The parameter α accounts for the shape of the organism and its swimming direction. The special cases of $\alpha = 1$ and -1 correspond to long, rod-shaped organisms, with $\alpha = 0$ corresponding to a spherical swimmer [Fig. 2(b)]. The swimming direction is parallel to (perpendicular to) the long axis for $\alpha > 0$ ($\alpha < 0$). It is notable that a small segment of a reaction front propagating in a fluid flow [Fig. 2(c)] can be modeled as an active particle[11,12] with $\alpha = -1$; in fact, the problem of reaction fronts moving in a fluid flow is a special case of the more general self-propelled particle problem.

The motion of an active particle in a flow is governed by the following set of differential equations:[14,25,29,38]

$$\dot{x} = u_x + V_0 \cos\theta, \quad \dot{y} = u_y + V_0 \sin\theta, \tag{1}$$

$$\dot{\theta} = (1+\alpha)(\omega/2) - \alpha\left(2\frac{\partial u_x}{\partial x}\cos\theta\sin\theta - \frac{\partial u_x}{\partial y}\cos^2\theta + \frac{\partial u_y}{\partial x}\sin^2\theta\right).$$

In these equations, u_x and u_y are the x- and y-components of the imposed velocity field and $\omega = \frac{\partial u_y}{\partial x} - \frac{\partial u_x}{\partial y}$ is the vorticity.

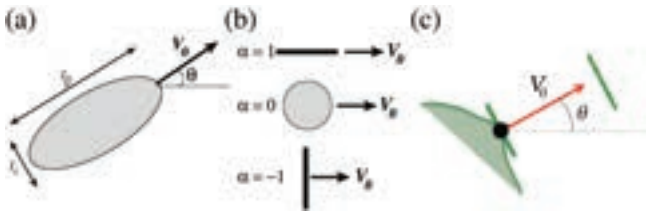

FIG. 2. (a) Model of an ellipsoidal swimmer in a flow. (b) Special cases for $\alpha = 1$, 0, or -1. (c) Model of an element of a reaction front in a flow.

For a self-propelled particle swimming with a constant speed V_0, chaotic trajectories are theoretically possible even for time-*independent*, 2D flows. The direction of swimming [Fig. 2(a)] must be specified in any phase space description of its motion, providing the third phase space dimension needed for chaotic motion.

III. EXPERIMENTAL TECHNIQUES

A. Flow

The flow is a laminar, 2D, time-independent chain of alternating vortices (Fig. 3). We generate the flow experimentally using magnetohydrodynamic[46,50] forcing (Fig. 4): a 1–2 mA electrical current [red arrows in Fig. 4(b)] passing through a channel with cross section $1.0 \times 1.0\,\text{mm}^2$ interacts with a spatially alternating magnetic field from a pattern of 1.0 mm-wide Nd–Fe–B magnets below the flow channel, producing alternating forces [blue arrows in Fig. 4(b)] across the channel. The result is a chain of vortices with no-slip boundary conditions and maximum speed U ranging from 300 to 800 μm/s. One unit cell of the resulting velocity field (measured using particle tracking velocimetry) is shown in Fig. 4(d).

Throughout this article, we use non-dimensional units where distances are scaled by the vortex width $L = 1.0$ mm such that y varies from 0 to 1.0 across the channel and x increments by 1.0 across each vortex. Time is scaled by the advection time L/U. The non-dimensional swimming speed is given by $v_0 = V_0/U$, where V_0 is the speed at which the microbe swims in the absence of a flow.

B. Microbes

The microbes (Fig. 5) used in the experiments are *Tetraselmis*, purchased from Carolina Biological Supply (Catalog No. 152610). Tetraselmis are marine, eukaryotic algae that are almost circular with a typical diameter of 10–15 μm. They are propelled by four pulling flagella. We mix 1 ml of the purchased sample with 150 ml of "Alga-Gro Seawater" in a flask with constant stirring. The mixture is cultured for 2 weeks under a dedicated fluorescent lamp. The stirrers are then turned off so that sessile microbes settle to the bottom, and most of the remaining culture is transferred to 15 ml centrifuge tubes.

The *Tetraselmis* microbes are dyed with fluorescein diacetate (FDA),[51,52] which causes *only* living organisms in the fluid to fluoresce, significantly enhancing the contrast during imaging and tracking. To tag the microbes using FDA, we start by dissolving approximately 0.015 g of FDA into 2 ml of acetone by shaking. Using a 10 μ; pipet, we add one drop of the FDA/acetone solution into 10 ml of the cultured *Tetraselmis* and wait 15–20 min. During this time, the FDA molecules diffuse through the lipid bilayers into the microbes, and enzymes within the microbes cleave the FDA molecules to create fluorescein. After this time, the *Tetraselmis*—and *only* living *Tetraselmis*—fluoresce. We then have

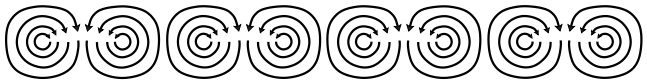

FIG. 3. Sketch of alternating vortex chain flow.

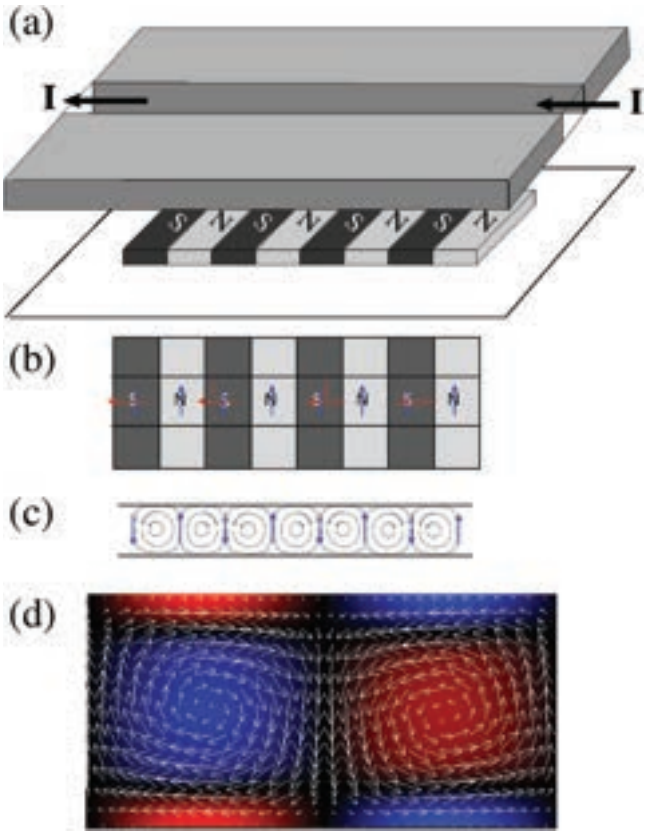

FIG. 4. (a) Exploded view of experimental apparatus, showing magnetohydrodynamic forcing technique. The channel has a width and height of 1.0 mm, and the magnets are 1.0 mm wide, resulting in vortices that measure 1.0 × 1.0 mm^2 with a depth 1.0 mm. (b) MHD forcing, as viewed from above. (c) Sketch of resulting vortex chain. (d) Experimentally measured velocity field (arrows) for a pair of vortices in the chain, along with vorticity denoted by blue (clockwise) and red (counterclockwise) colors.

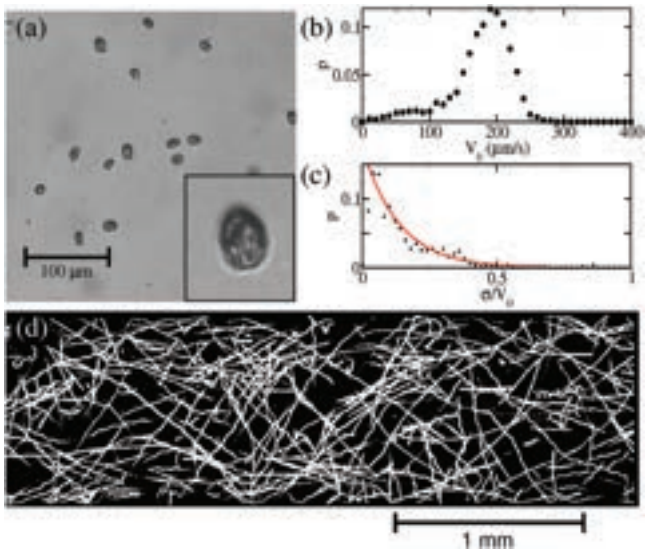

FIG. 5. (a) Image of *Tetraselmis* microbes used in these experiments, imaged with a microscope with 40× magnification. The inset is a zoom-in of one of the microbes. (b) Distribution of average swimming speeds for the *Tetraselmis* in the absence of a fluid flow. (c) Distribution showing the variation of swimming speeds for individual microbes, plotted as the ratio of the standard deviation and average (mean) swimming speeds for a microbe. The red curve is a fit with functional form $p = ae^{-b\sigma/V_0}$ with $a = 0.17$ and $b = 7.3$. (d) Streak image showing 10 s of movement of microbes in the apparatus in the absence of a flow.

approximately 30 min to run the experiments with this fluorescently tagged *Tetraselmis* using epifluorescence microscopy, after which much of the fluorescein has diffused back out from the microbes into the surrounding fluid, reducing the contrast.

The use of FDA does not seem to have a significant effect on the swimming of the microbes. We have also conducted tests that indicate that imposed magnetic fields (without electrical current) and imposed currents (without magnetic fields) have negligible effect on the swimming properties of the *Tetraselmis*. The density of the microbes is relatively low, no more than about 20 microbes per mm^2, with a typical separation between microbes of around 200 μm, or about 15–20 microbial body lengths; consequently, collisions between the swimming Tetraselmis microbes are not expected to affect the results significantly.

In the experiments, the microbes are imaged with epifluorescence on a Nikon Eclipse microscope with a 2× or 4× objective. With these magnifications, the field of view is slightly more than 6 vortices or 3 vortices for the 2× and 4× objectives, respectively. (Measurements of variance for long-range transport are done with data collected with the 2× objective since the field of view is wider.) A streak image is shown in Fig. 5(d) showing 10 s of movement of the microbes in the apparatus with no vortex flow. There is a range of swimming behavior, including straight-line (smooth) motion, swimming with tumbling, and oscillatory behavior which is likely a two-dimensional projection of helical swimming.[53] In the absence of a fluid flow, the microbes swim with an average speed that varies roughly from 150 to 250 μm/s [Fig. 5(b)]; individual microbes swim with typical speed variations [Fig. 5(c)] that are 0.14 of the average speed.[31]

C. Tracking and analysis

We acquire images of the algae in the flow with an Andor Zyla sCMOS camera connected to the microscope. A background image is determined by averaging images for half a minute. We subtract this background image in real time from each subsequent image. We threshold the subtracted images and store to disk the coordinates and intensities in each image for pixels above the threshold. With this approach, we are able to store information at a rate of 30–50 frames per second for arbitrarily long durations. We then track microbes from the stored data in IDL with a package[54] that determines centroid coordinates for clusters of pixels (with each cluster identified as a microbe) and then links coordinates in successive frames to determine trajectories.

We fit the $x(t)$ and $y(t)$ coordinates of each trajectory to sliding parabolas and take derivatives to determine the x- and y-components of the total velocity $\vec{V}_{traj}$ of each microbe as it moves through the flow. To determine the swimming velocity $\vec{V}_s$ of a specific microbe in an imposed flow, we subtract the experimentally measured flow velocity $\vec{u}_{flow}$ from the velocity of the overall trajectory: $\vec{V}_s = \vec{V}_{traj} - \vec{u}_{flow}$. From the swimming velocity, we determine the instantaneous swimming speed V_s and swimming direction $\theta = \arctan(V_{sy}/V_{sx})$. To compare with the theoretical predictions, we approximate V_0 by the average of the swimming speed over its trajectory: $V_0 = \langle V_s \rangle$. The dimensionless swimming speed is then given by $v_0 = V_0/U$, where U is the maximum flow speed. Trajectories are grouped into different v_0 bins for theory comparison: $v_0 = 0.2$, 0.3, 0.4, or 0.5. The maximum deviation of a trajectory's v_0 from its bin's value is 0.05 (e.g., if $0.15 \leq v_0 < 0.25$, then the trajectory is classified into the $v_0 = 0.2$ bin).

IV. NUMERICAL SIMULATIONS

To support and interpret the experimental data, we simulate the motion of a self-propelled tracer [using Eq. (1)] in a time-independent, 2D vortex chain flow (Fig. 3). α used for the simulations is 0.3, which corresponds approximately to the body shape of the real microbes used for experiments. This simplified model assumes that the microbes swim with no active tumbling or rotational diffusion, rotating only because of interactions with the flow. Furthermore, we do not account for the effects of the flagella on the shape parameter α. For the velocity field, we approximate the vortex chain flow by using the 2D velocity field derived previously[55] to model a similar vortex flow with no-slip boundary conditions.

Two simulated trajectories for non-dimensional swimming speed $v_0 = 0.4$ are shown in Fig. 6(a). The trajectories start with identical initial positions $(x_0, y_0) = (3.0, 0.3)$ but with *slightly* different swimming orientations ($\theta_0 = 3.30$ and 3.34 radians). The trajectories follow each other closely for short times, but then dramatically diverge, consistent with sensitive dependence on initial conditions, a hallmark of chaotic trajectories.

The chaotic nature of active tracer trajectories in the vortex flow is reinforced by plotting Poincaré sections.[35,45] For each simulated trajectory, we plot the (x, y) coordinate each time the trajectory crosses $\theta = 0$ in the positive direction (from negative to positive θ). The resulting Poincaré sections are shown in Figs. 6(b)–6(e) for $v_0 = 0.2$, 0.3, 0.4, and 0.5, respectively. The seemingly random scattering of points from a single trajectory [black dots in each of Figs. 6(b)–6(e)] indicates chaotic trajectories in those regions. For $v_0 = 0.2$, there is a sizable region near the top with trajectories that remain localized, following an ordered, repeatable pattern. Note, however, that the trajectory (green dots) that starts near the outside of this region escapes into the chaotic region, indicating that this may be a chaotic trajectory that is dynamically trapped to the edge of the ordered region. The ordered region for $v_0 = 0.2$ disappears for larger v_0, although there is still temporary sticking in that region as seen with the red and green dots for $v_0 = 0.3$ [Fig. 6(c)]. There are two very small ordered regions for the cases with $v_0 = 0.3$ and 0.4 (in the shape of two eyes and a mouth, in blue), and there appear to be no ordered regions for $v_0 = 0.5$.

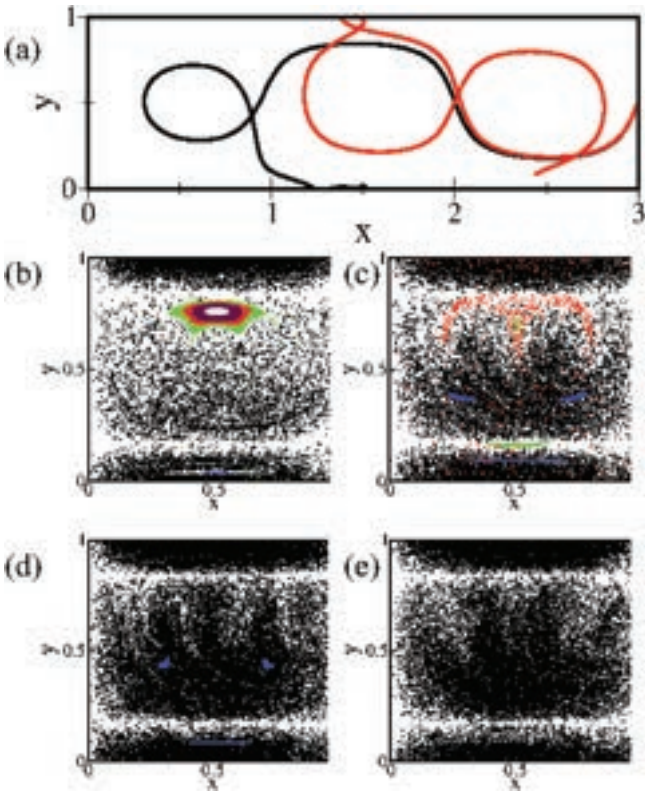

FIG. 6. (a) Two simulated trajectories for $v_0 = 0.4$; both start from the same initial position $(x_0, y_0) = (3.0, 0.3)$ but with different initial swimming orientations $\theta_0 = 3.30$ and 3.34 radians. Simulated Poincaré sections for v_0 equal to (b) 0.2, (c) 0.3, (d) 0.4, and (e) 0.5. For each Poincaré section, every point with the same color is from the same simulated trajectory.

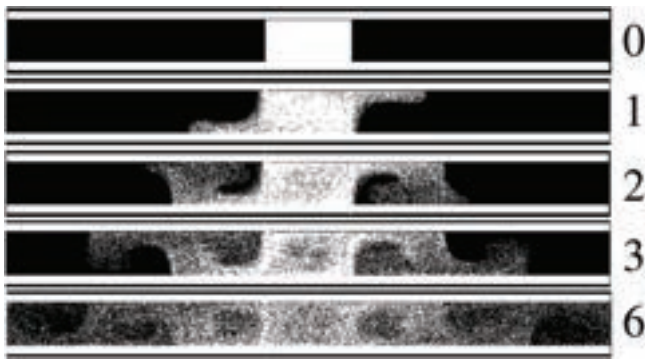

FIG. 7. Simulations showing long-range transport of swimmers in a 7-vortex chain. White dots are the individual swimmers, with the middle vortex initially filled. The numbers denote the nondimensional time tU/L after the start of the simulation.

The model of Eq. (1) is not volume-preserving for $\alpha \neq 0$, resulting in density variations[25] in the Poincaré sections. The slight non-volume-preservation also results in the eventual escape—after a long time—even of trajectories starting in the ordered regions. The reverse is not observed in the simulations, as black dots in the chaotic sea do not penetrate into the ordered regions.

Swimmers in the chaotic regions not only mix within each vortex in the simulations (excluding the ordered regions) but also cross the boundaries between adjacent vortices. In a previous paper,[31] we demonstrated *swimming invariant manifolds* (SwIMs) that act as barriers blocking motion of active particles in laminar flows. For the vortex chain flow, the SwIMs combine to form "chutes" that account for the mixing between vortices. The result is that an ensemble of swimmers initially in one vortex spreads throughout the vortex chain, as shown numerically in Fig. 7.

V. EXPERIMENTAL RESULTS

A streak image of microbes swimming in the vortex flow is shown in Fig. 8(a). The vortex flow is readily visible in this image, as is the fact that the microbes are swimming relative to the flow, indicated by the crossing of the trajectories and motion of microbes between vortices, behavior that would not be possible if the particles were passive.

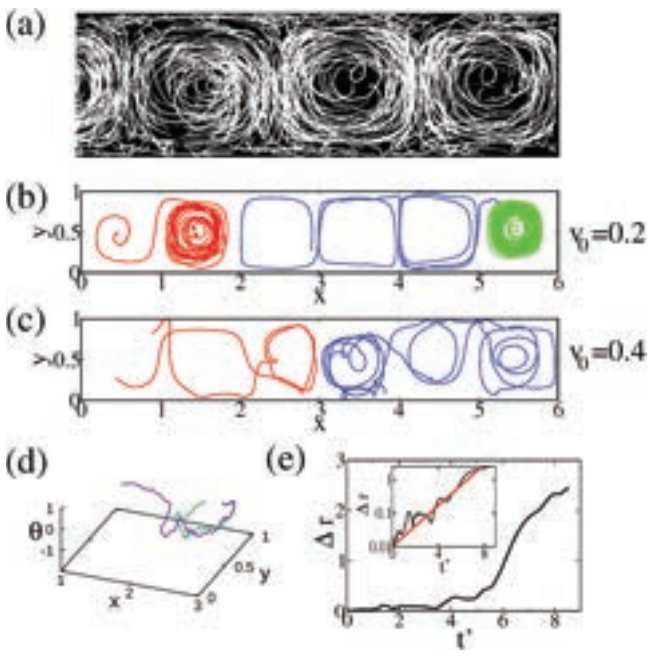

FIG. 8. (a) Streak image showing 10 s of motion of microbes in 3.5 vortices in the flow; magnification 4×. (b) Examples of experimental microbe trajectories with non-dimensional swimming speed $v_0 = 0.2$. (c) Trajectories of microbes with $v_0 = 0.4$. (d) Two different pieces of the red trajectory from (c), displayed in 3D, (x, y, θ) space. The two trajectory pieces start at virtually the same initial (x_0, y_0, θ_0) but diverge at later times. (e) Separation in (x, y, θ) phase space between the two trajectories in (d); the inset plots the separation in a semi-logarithmic graph, illustrating the roughly exponential separation in time.

Examples of experimental trajectories for microbes swimming with non-dimensional speed $v_0 = 0.2$ are shown in Fig. 8(b). Many of the trajectories remain confined to a single vortex, similar to the green trajectory at the right (which is one of the longest-duration trajectories that we were able to track), although trajectories near the vortex edges cross between vortices in the chain (blue and red trajectories). The red trajectory shows an example of what dynamic trapping looks like in the experimental data—the trajectory circles the vortex near the vortex edge (but not all the way out) for an extended period of time, producing a dense band in the image. Elements of non-smooth swimming are also visible in these trajectories, including rocking behavior (the slight wiggles in the red trajectory), some subtle active tumbling in the blue trajectory, and some clear noise throughout in the swimming.

The trajectories are quite different for larger swimming speeds [Fig. 8(c)]. Trajectories move more freely through and between the vortices, and loops in the trajectories are more prevalent than for the smaller swimming speeds. Noise and tumbling are more visible in these trajectories since the swimming is faster compared to the flow. Between tumble events, there are segments where the behavior appears to be fairly smooth.

For each run, we examine the swimming angles θ determined from the velocity subtraction approach discussed above, looking for instances where $d\theta/dt$ significantly exceeds the value predicted from the $\dot{\theta}$ equation in Eq. (1). We label these rapid $\dot{\theta}$ events as active tumbles and cut the trajectory into smooth-swimming segments before and after the tumble events. In this way, we can treat these segments as new trajectories with most active tumbling removed.

The red curve in Fig. 8(c) shows sensitive dependence on initial conditions, similar to that seen in the simulations [Fig. 6(a)]. The trajectory happens to return to virtually the same (x, y) coordinate near the top of the vortex between $x = 2$ and 3. We plot two segments of this trajectory in (x, y, θ) space in Fig. 8(d) starting from that common location. Consistent with deterministic chaos, these two trajectory segments that start at almost the same initial (x, y, θ) coordinates follow each other for short times and then diverge significantly, with one crossing into the next vortex while the other circles back. The separation between these two segments grows roughly exponentially when coarse-grained [Fig. 8(e)], similar to the expected (coarse-grained) exponential separation $\Delta r(t) \approx \Delta r_0 e^{\lambda t}$ for chaotic trajectories.[56] Of course, since the swimming of the microbe is not perfectly smooth, this plot in itself is not proof of deterministic chaos. However, this behavior is common in these experiments and is highly indicative of chaotic behavior.

Since the system of differential equations in Eq. (1) is not volume-conserving for $\alpha \neq 0$, density variations are possible over time. Figure 9 shows (x, y) slices of histograms of the trajectories around swimming direction $\theta = 0$, $\pi/2$, π, and $3\pi/2$ for v_0 of both 0.2 and 0.4. Significant variations in the density are visible for $v_0 = 0.2$. This is another manifestation of sticking in this system for small v_0. In fact, the regions of high density in the $\theta = 0$ and π slices for $v_0 = 0.2$ coincide approximately with the location of the ordered island in the simulated Poincaré sections [Fig. 6(b)]. Smooth-swimming microbes moving in the chaotic region with no Brownian motion in a noise-free flow should never penetrate into an

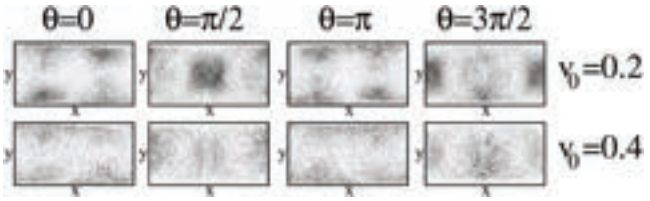

FIG. 9. Histograms of (x, y) coordinates for swimming microbes with $v_0 = 0.2$ (top) and $v_0 = 0.4$ (bottom); slices around $\theta = 0$, $\pi/2$, π, and $3\pi/2$. In these images, x goes from 0 to 2 (starting and finishing at vortex edges) and y goes from 0 to 1.

ordered island. With the noise and tumbling, however, microbes in the experiments are able to enter the theoretically predicted ordered region and then remain stuck for a finite period, resulting in a higher density in that region.

The one-dimensional variance $\langle x^2 \rangle$ calculated from the experimentally measured trajectories is shown in Fig. 10 for both the cases with the most significant active tumbling events removed [Fig. 10(a)] and with all of the data including the active tumbling [Fig. 10(b)]. For small times, the variance with reduced-tumbling trajectories [Fig. 10(a)] grows roughly ballistically, i.e., $\langle x^2 \rangle \sim t^\gamma$ with $\gamma \approx 2$. At a time comparable to typical vortex circulation times, the variance curve bends over. For $v_0 = 0.2$ and 0.3, the transport becomes subdiffusive: $\langle x^2 \rangle \sim t^\gamma$ with $0 < \gamma < 1$ (see Table I). At higher swimming speeds, the variance growth is consistent with diffusive-like transport, where $\gamma = 1$.

The growth of the variance with active tumbling [Fig. 10(b)] at low swimming speed regimes ($v_0 = 0.2$ and 0.3) is still subdiffusive after the initial ballistic transient (Table I), though the growth exponent γ is closer to that for diffusive behavior ($\gamma = 1$). At higher swimming speed regimes, the transport is diffusive and potentially even slightly superdiffusive ($\gamma > 1$) for $v_0 = 0.5$.

Although not central to our conclusions, we have also compared the apparent tumbling behavior of the microbes with and without the imposed vortex flows. Probability distribution functions of run times and tumbling angles are plotted in Fig. 11, revealing exponential and roughly power-law relations for the run time and tumble angle distributions, respectively. The analysis indicates that the addition of the flow increases the tumbling (reducing the run times), as evident by the lowered curve of run distribution in the vortical trajectories. The tumble angle distribution also skews smaller in the case with flow, indicating perhaps that these are small-duration tumbles that do not reorient the microbes too much. There remain questions about whether this effect is due to more active tumbling of the microbe when in the presence of the flow, or to larger noise in the determined microbe orientations from velocity subtraction (see Sec. III C), which could register as tumbles. The analysis of our data also implies that there is a preference for the microbes to tumble in a direction opposite the rotation of the organism due to the flow. Additional experiments and analysis are needed to quantify the effects that imposed flows have on the tumbling of the microbes.

TABLE I. Slopes for best fit lines from Fig. 10.

v_0	Reduced tumbling	All trajectories
0.2	0.23 ± 0.03	0.57 ± 0.04
0.3	0.69 ± 0.03	0.76 ± 0.02
0.4	1.05 ± 0.03	1.08 ± 0.06
0.5	1.11 ± 0.07	1.22 ± 0.04

VI. LAGRANGIAN-AVERAGED TRAJECTORIES AND STICKING PROBABILITIES

Determination of Poincaré sections and sticking time probabilities from experimental data is difficult since both of these measures require long-duration trajectories. That problem is particularly challenging for tracking of self-propelled particles since they can swim out of the focal plane, limiting the duration of tracked trajectories.

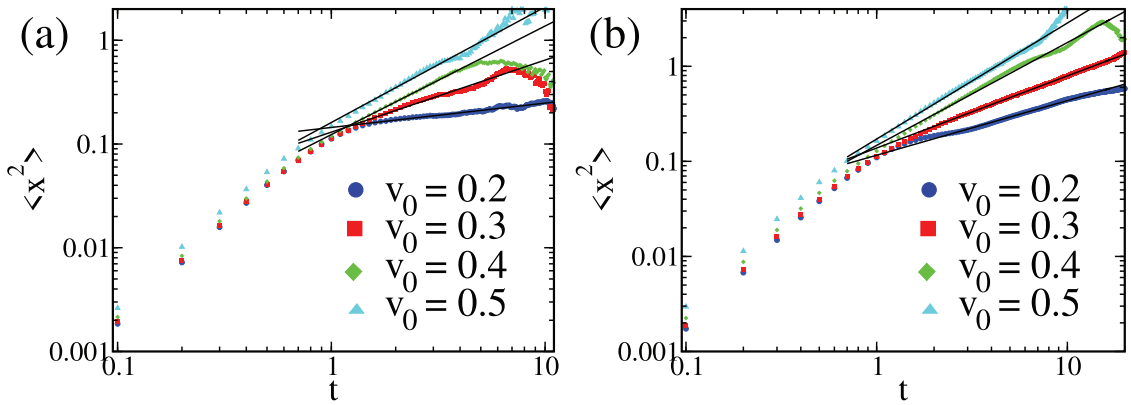

FIG. 10. Variance calculated from the experimental trajectories. (a) Reduced-tumbling trajectories and segments. (b) All of the trajectories, including the most significant active tumbling events. For each plot, the non-dimensional average swimming speed v_0 is 0.2 (dark blue circles), 0.3 (red squares), 0.4 (green diamonds), and 0.5 (light blue triangles). Best fit curves are shown as black lines.

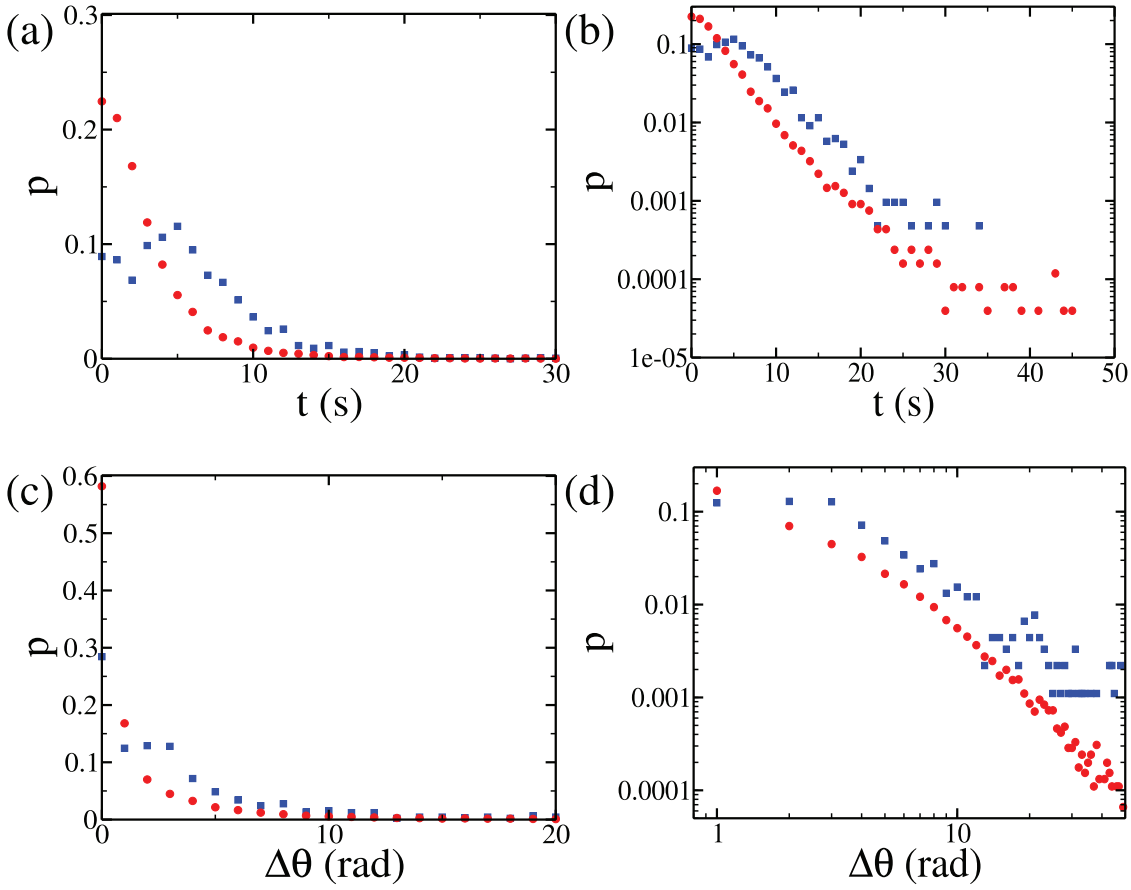

FIG. 11. (a) Experimentally determined probability distribution functions (PDFs) of run times between tumbles. (b) Same PDFs as in (a) but plotted semi-logarithmically. (c) Probability distributions of tumble angles $\Delta\theta$. (d) Same as in (c) but plotted logarithmically in both $\Delta\theta$ and p. In all of the plots, the data corresponding to no flow are shown with blue squares, and the data corresponding to the vortex flow are shown with red circles.

(Also, we cannot confine the motion to 2D with the use of a narrow cell because microbes typically swim very differently near solid boundaries.[57,58])

We probe our experimental data more deeply by calculating what we call *Lagrangian-averaged trajectories* (LATs). The approach is illustrated in Fig. 12(a) and in LATapproach.mp4 in the supplementary material. Starting from a chosen initial condition (x_0, y_0, θ_0) [red dot labeled "start" in Fig. 12(a)], we search for trajectories and trajectory segments of microbes that start in a small box around (x_0, y_0, θ_0) and that are swimming with a chosen nondimensional speed v_0 (blue dots). We then determine the locations of each of those trajectories after a time interval Δt (green dots) and then do a weighted average of those points [weighted by distance between the blue starting location and the location (x_0, y_0, θ_0)] to determine the next point (x_1, y_1, θ_1) in the LAT. The process is then repeated over and over again to assemble a trajectory that reflects an average of the experimentally measured trajectories.

When averaging the coordinates [green dots in Fig. 12(a)], we cannot simply use the (x, y) coordinates of the individual points. If the points are distributed along an arc around a vortex, a simple spatial averaging can result in an averaged coordinate [red dots in Fig. 12(a)] that is closer to the vortex center than the individual points. To avoid this problem, we first convert the coordinates from (x, y) to (ψ, θ). The coordinate ψ is the value of the streamfunction[35] at the point (x, y) defined such that ψ is -1 or $+1$ at the centers of clockwise (CW) circling and counterclockwise (CCW) circling vortices, respectively; $\psi = 0$ around the edges of all of the vortices. The coordinate θ is the angle of the microbe location relative to the center of the vortex, defined as clockwise from the positive x axis for CW vortices and counterclockwise from the negative x axis for CCW vortices. These definitions are chosen so that the coordinates (ψ, θ) remain continuous crossing from one vortex to the next.

The use of Lagrangian-averaged trajectories has a couple of benefits: (a) arbitrarily long trajectories can be obtained, overcoming the limitations of limited-time trajectories described above; and (b) the averaging can conceivably smooth out some of the effects of noise in the swimming of the microbes. (We use the tumbling-minimized trajectories and trajectory segments in

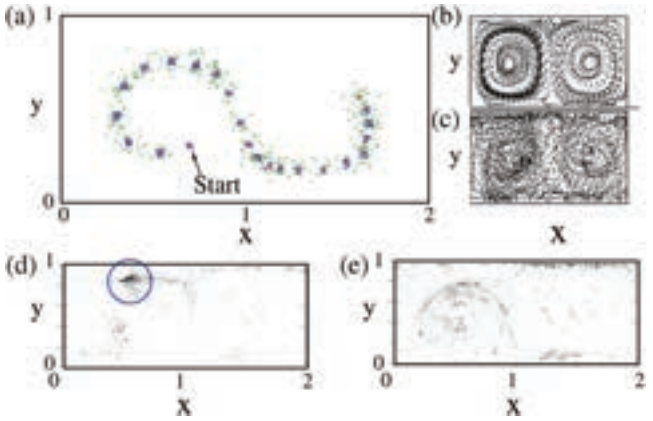

FIG. 12. (a) Illustration of the technique to calculate *Lagrangian-averaged trajectories* (LATs). Examples of LATs for (b) $v_0 = 0.2$; and (c) $v_0 = 0.4$. In both (b) and (c), LATs are displayed as projections in (x, y) with x varying from 0 to 2 and y from 0 to 1. Density plots of Poincaré sections calculated from LATs for (d) $v_0 = 0.2$ and (e) $v_0 = 0.4$.

the LAT calculations.) We considered (and attempted) using an approach similar to that used for some transport-related studies[17,59] where measurements of the instantaneous velocity fields are made and trajectories are calculated numerically from those experimentally measured velocity fields. We could measure (u_x, u_y, u_θ) "velocity" fields experimentally and determine trajectories in (x, y, θ)-space numerically from these velocity fields. However, (a) the LAT method uses more data from the experimentally measured trajectories (since this does not use just the instantaneous velocity field); (b) there is no need to do any numerical integration with LATs; and (c) determining a (u_x, u_y, u_θ) field is hampered by regions in (x, y, θ)-space where microbe trajectories avoid (see Fig. 9), an issue that does not hamper the calculation of LATs.

We partially benchmark the LAT approach by using numerical simulations for which the velocity field is known and where the motion of swimmers is not affected by noise and tumbling seen in the experiments. Instead of using experimentally determined trajectories and segments, we generate swarms of numerically simulated trajectory segments at random locations and calculate LATs starting from a chosen initial position from these simulated trajectory segments. (We use the same averaging parameters for this numerical benchmarking as those used to calculate LATs from the experimental trajectories.) We then compare the resulting benchmark LATs to long-duration trajectories starting from the same initial location, simulated numerically from Eq. (1). LATs calculated starting in the ordered region in Fig. 6(b) show ordered behavior similar to the numerical trajectories used to plot Fig. 6(b), and LATs calculated starting in the chaotic region show chaotic behavior similar to the full numerical trajectories starting at the same locations. The LATs follow the simulated trajectories well for short times but deviate slightly for longer times in the ordered region and deviate significantly in the chaotic region, which is to be expected since chaotic trajectories are sensitive to small deviations in the initial conditions. Note that this benchmarking does not account for noise and tumbling of the microbes.

Figures 12(b) and 12(c) show (x, y) projections of individual LATs calculated from the experimental data with $v_0 = 0.2$ and 0.4, respectively. The sticking behavior for $v_0 = 0.2$ hinted at in Figs. 8(b) and 9 shows up as a notably high-density band in the left vortex of the LAT shown in Fig. 12(b). These high-density bands are common for LATs for $v_0 = 0.2$, but are absent for LATs determined from the $v_0 = 0.4$ data [Fig. 12(c)].

Poincaré sections are shown in Figs. 12(d) and 12(e). These are determined from 1320 experimental LATs, each launched from vertical strips near the edges of the first vortex (in regions $0 < x < 0.2$ and $0.8 < x < 1.0$) with a spray of different initial angles. There is a region near the top of the left vortex [circled in blue in Fig. 12(d)] with a significantly higher density of points in the Poincaré section for $v_0 = 0.2$. This corresponds to the region in (x, y) where the dense band of trajectories similar to that in Fig. 12(b) crosses the plane $\theta = 0$. Although there are variations in density for the Poincaré section for $v_0 = 0.4$ [Fig. 12(e)], there is no region where the trajectories return repeatedly in successive iterations.

We use the Poincaré sections calculated from the LATs to determine experimental trapping number and trapping time probabilities. For each trajectory, if a point (x_i, y_i, θ_i) in the Poincaré section is within a defined distance r_s of the previous Poincaré iterate $(x_{i-1}, y_{i-1}, \theta_{i-1})$ and if the time between Poincaré iterates $i - 1$ and i is less than a threshold circulation time, then the microbe is considered to be trapped during the interval between $(i - 1)$ and i. We choose a sticking distance $r_s = 0.3$ in dimensionless units where the distance is scaled by a vortex width and θ is scaled by 1 radian. This sticking distance is comparable to the size of the ordered island found in simulations for $v_0 = 0.2$ [Fig. 6(b)]. If the microbe *is* dynamically trapped, it should return in a time comparable to a typical circulation time. We, therefore, choose a threshold time $t_c = 7$, comparable to two circulation times on the assumption that if it takes longer than that for the microbe to return, it is not due to dynamic trapping. Note also that this approach captures trapping behavior regardless of the location of the trapping region in (x, y).

Probabilities that a trajectory is stuck for n consecutive Poincaré iterates or for a total duration t are shown in Fig. 13. There is significantly more and longer trapping intervals for the microbes

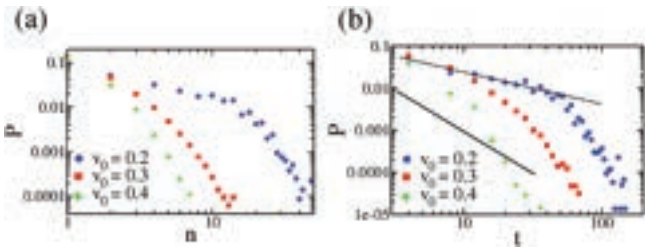

FIG. 13. Sticking probabilities calculated from LATs in terms of (a) number n of Poincaré iterations and (b) sticking time. For both (a) and (b), blue circles, red squares, and green diamonds correspond to $v_0 = 0.2$, 0.3, and 0.4, respectively. In (b), the top black line is a best fit to the small-time regime for $v_0 = 0.2$ and the bottom black line shows a reference slope of -2.

swimming with $v_0 = 0.2$ than for $v_0 = 0.3$ or 0.4, and the trapping occurs in the region near the top of the left vortex, consistent with the location of the ordered island in Fig. 6(b). For the data with non-dimensional swimming speed $v_0 = 0.2$, there is a regime of power-law behavior with $P(t) \sim t^{-\nu}$ with $\nu = 0.76 \pm 0.03$ for times up to several typical circulation times; for longer sticking times, $P(t)$ transitions to a tail with a much steeper slope. [The scaling is similar if we calculate $P(t)$ with $r_s = 0.2$ or 0.1, although the transition to a steeper slope occurs at smaller times for smaller r_s.] The trapping time probability distribution for $v_0 = 0.3$ does not have clear power-law scaling. For small sticking times, a semi-log plot decreases with a slope between -1 and -2; for non-dimensional time above 10, the slope exceeds -2. There is very limited sticking for $v_0 = 0.4$ as the drop-off with t has a slope that exceeds -2 at all times. These sticking time probabilities and the variance results from Fig. 10(b) and Table I are consistent with theoretical studies[43,60,61] that predict subdiffusion ($\gamma < 1$) for systems where trajectories stick to localized regions with a power-law distribution with $\nu < 2$ and normal (enhanced) diffusion for sticking time probability distributions that decay with t faster than $P(t) \sim t^{-\nu}$ with $\nu = 2$. (The decay exponent ν for the $v_0 = 0.2$ case is actually lower than the minimum of $\nu = 1$ in the theoretical predictions.)

VII. DISCUSSION

We interpret the significantly enhanced trapping times for the slower swimmers ($v_0 = 0.2$ and 0.3) in the experiments as due to dynamic trapping of microbes to the islands of ordered trajectories predicted by the idealized numerical model [Fig. 6(b)]. The mechanism for dynamic trapping in these experiments likely differs from the mechanism[40] discussed in Sec. II A. Instead of sticking to the perimeter of the ordered region for $v_0 = 0.2$ or 0.3, the microbes appear to be passing *into* the islands, crossing the supposedly impenetrable KAM invariant tori. Penetration of the idealized KAM tori is due likely to the fact that the real microbes do not swim perfectly smoothly; the swimming speeds are not constant, and noise, rocking and imperfections (not accounted for in the tumbling reduction analysis) in the swimming cause changes in the swimming direction beyond those due to interactions with the flow. Once inside the island, the microbes remain stuck until noise in the swimming speed and/or direction enables them to escape. As seen in the simulations, the non-volume-preserving property of the phase space for non-spherical swimmers can also enable them to escape islands.

When significant active tumbling is included [Fig. 10(b) and right column of Table I], the growth exponent γ is closer to 1 for swimming speeds $v_0 = 0.2$ and 0.3. Active tumbling clearly reduces the sticking times, consistent with the predictions of a growth in the variance that is closer to diffusive. The slight superdiffusive behavior found for the active tumbling data with swimming speed $v_0 = 0.5$ is likely not due to dynamic trapping; it is possible that the motion of the microbes along the walls[57,58] could be giving rise to flights[41,42] that are responsible for the slight superdiffusion.

The sub-diffusion that results from noisy dynamical trapping is similar in many respects to subdiffusion found for microbes swimming in a tightly packed porous system.[1] In those studies, microbes are trapped temporarily in cavities within the porous medium, hopping sporadically to other trapped regions. The subdiffusion seen in our experiments is also due to a hop-and-trap mechanism; however, the trapping here is not due to a physical restriction but rather to the dynamic trapping of noisy swimmers to transport structures. The same dynamic trapping mechanism could also result in superdiffusive transport ($\gamma > 1$) in flows where smooth-swimming microbes have ordered regions with long-range trajectories, similar to superdiffusion seen for passive tracers in laminar flows with long-range jets.[42,48,60]

Our experiments demonstrate that deterministic chaos can have a measurable impact on the transport properties of real, swimming organisms, even if there is noise in the system, either from the fluctuations in the swimming speeds or directions (as in these experiments) or presumably in the flow itself. Since the chaotic signatures are not dependent on the system being completely noise-free, we expect similar dynamic trapping behavior and anomalous diffusion in the mixing of active particles in a wide range of systems including: (a) dynamic trapping of bacteria swimming in the blood stream, especially in vortex regions behind obstructions in the arteries, a mechanism that could contribute to the onset of endocarditis; (b) dynamic trapping of microbes in air passageways in the human body, especially in the lungs; and (c) dynamic trapping of self-propelled particles in larger-scale, coherent vortices in oceanic and atmospheric flows. For oceanic-scale flows, microbes that are dynamically trapped behave more like passive tracers since their swimming speeds are much smaller than flow speeds. However, larger-scale organisms (birds, fish, sharks) and human-built vessels (ships and planes) could experience dynamic trapping as active tracers in larger-scale flows.

Additional studies are needed on the dynamic trapping of active particles to islands in the presence of noise. In particular, theory is needed to be able to predict the form and decay exponents of sticking probability distributions, given a fluid flow and a characterization of the swimming behavior of the microbes and any noise in the system. Careful studies are also needed to consider differences between random noise in the swimming and effects of active tumbling. Additional studies are also needed to assess the effect of varying shape (and, therefore, variations in the shape parameter α) on dynamic trapping.

SUPPLEMENTARY MATERIAL

See the supplementary material for the multimedia (video) of the approach used to determine Lagrangian-averaged trajectories (LATs). This is basically a video of the method shown in Fig. 12(a).

ACKNOWLEDGMENTS

These experiments were supported by the National Science Foundation (NSF) under Grant Nos. DMR-1806355 and DMR-2302708. The authors would like to thank Jack Raup, Joe Tolman, and Brian Garthwaite for their assistance with the microfluidic cells.

AUTHOR DECLARATIONS

Conflict of Interest

The authors have no conflicts to disclose.

Author Contributions

N.L. and T.H.S. conceived and developed the experimental techniques; N.L. performed experiments; N.L. and T.H.S. analyzed data and interpreted the results; N.L. and T.H.S. wrote the paper.

Nghia Le: Conceptualization (equal); Formal analysis (equal); Investigation (equal); Methodology (equal); Software (equal); Validation (equal); Visualization (equal); Writing – original draft (equal); Writing – review & editing (equal). **Thomas H. Solomon:** Conceptualization (equal); Formal analysis (equal); Funding acquisition (lead); Investigation (equal); Methodology (equal); Project administration (lead); Software (equal); Validation (equal); Visualization (equal); Writing – original draft (equal); Writing – review & editing (equal).

DATA AVAILABILITY

The data that support the findings of this study are available from the corresponding author upon reasonable request.

REFERENCES

[1]T. Bhattacharjee and S. S. Datta, "Bacterial hopping and trapping in porous media," Nat. Commun. **10**, 2075 (2019).
[2]A. Apolloni, C. Poletto, and V. Colizza, "Age-specific contacts and travel patterns in the spatial spread of 2009 H1N1 influenza pandemic," BMC Infect. Dis. **13**, 176 (2013).
[3]K. Khan, J. Arino, W. Hu, P. Raposo, J. Sears, F. Calderon, C. Heidebrecht, M. Macdonald, J. Liauw, A. Chan, and M. Gardam, "Spread of a novel influenza a (H1N1) virus via global airline transportation," N. Engl. J. Med. **361**, 212–214 (2009).
[4]A. Tsuda, R. Rogers, P. Hydon, and J. Butler, "Chaotic mixing deep in the lung," Proc. Natl. Acad. Sci. U.S.A. **99**, 10173–10178 (2002).
[5]T. Ishikawa, T. Sato, G. Mohit, Y. Imai, and T. Yamaguchi, "Transport phenomena of microbial flora in the small intestine with peristalsis," J. Theor. Biol. **279**, 63–73 (2011).
[6]J. Y. Yoo and Y. K. Lee, "Review—Transport phenomena associated with cells incurring diseases," J. Mech. Sci. Tech. **21**, 1855–1868 (2007).
[7]M. Sandulescu, C. Lopez, E. Hernandez-Garcia, and U. Feudel, "Biological activity in the wake of an island close to a coastal upwelling," Ecol. Complex. **5**, 228–237 (2008).
[8]D. Bastine and U. Feudel, "Inhomogeneous dominance patterns of competing phytoplankton groups in the wake of an island," Nonlinear Process. Geophys. **17**, 715–731 (2010).
[9]S. Bialonski, D. A. Caron, J. Schloen, U. Feudel, H. Kantz, and S. D. Moorthi, "Phytoplankton dynamics in the Southern California bight indicate a complex mixture of transport and biology," J. Plankton Res. **38**, 1077–1091 (2016).
[10]P. Gunnarson, I. Mandralis, G. Novati, P. Koumoutsakos, and J. O. Dabiri, "Learning efficient navigation in vortical flow fields," Nat. Commun. **12**, 7143 (2021).
[11]J. Mahoney, D. Bargteil, M. Kingsbury, K. Mitchell, and T. Solomon, "Invariant barriers to reaction front propagation in fluids flows," Europhys. Lett. **98**, 44005 (2012).
[12]D. Bargteil and T. Solomon, "Barriers to front propagation in ordered and disordered vortex flows," Chaos **22**, 094107 (2012).
[13]Marcos, H. C. Fu, T. R. Powers, and R. Stocker, "Bacterial rheotaxis," Proc. Natl. Acad. Sci. U.S.A. **109**, 4780–4785 (2012).
[14]A. Zöttl and H. Stark, "Nonlinear dynamics of a microswimmer in Poiseuille flow," Phys. Rev. Lett. **108**, 218104 (2012).
[15]A. J. T. M. Mathijssen, N. Figueroa-Morales, G. Junot, E. Clement, A. Lindner, and A. Zöttl, "Oscillatory surface rheotaxis of swimming *E. coli* bacteria," Nat. Commun. **10**, 3434 (2019).
[16]G. Haller, "Lagrangian structures and the rate of strain in a partition of two-dimensional turbulence," Phys. Fluids **13**, 3365–3385 (2001).
[17]G. A. Voth, G. Haller, and J. P. Gollub, "Experimental measurements of stretching fields in fluid mixing," Phys. Rev. Lett. **88**, 254501 (2002).
[18]A. Hadjighasem, M. Farazmand, D. Blazevski, G. Froyland, and G. Haller, "A critical comparison of Lagrangian methods for coherent structure detection," Chaos **27**, 053104 (2017).
[19]S. Balasuriya, N. T. Ouellette, and I. I. Rypina, "Generalized Lagrangian coherent structures," Physica D **372**, 31–51 (2018).
[20]R. Ran, Q. Brosseau, B. C. Blackwell, B. Qin, R. L. Winter, and P. E. Arratia, "Bacteria hinder large-scale transport and enhance small-scale mixing in time-periodic flows," Proc. Natl. Acad. Sci. U.S.A. **118**, e2108548118 (2021).
[21]R. Ran and P. E. Arratia, "Enhancing transport barriers with swimming microorganisms in chaotic flows," J. Fluid Mech. **988**, A25 (2024).
[22]X. Si and L. Fang, "Interaction between swarming active matter and flow: The impact on Lagrangian coherent structures," Phys. Rev. Fluids **9**, 033101 (2024).
[23]R. Rusconi, J. S. Guasto, and R. Stocker, "Bacterial transport suppressed by fluid shear," Nat. Phys. **10**, 212–217 (2014).
[24]S. A. Berman and K. A. Mitchell, "Swimming dynamics in externally driven flows: The role of noise," Phys. Rev. Fluids **7**, 014501 (2022).
[25]C. Torney and Z. Neufeld, "Transport and aggregation of self-propelled particles in fluid flows," Phys. Rev. Lett. **99**, 078101 (2007).
[26]A. Sokolov and I. S. Aranson, "Rapid expulsion of microswimmers by a vortical flow," Nat. Commun. **7**, 11114 (2016).
[27]J.-A. Arguedas-Leiva and M. Wilczek, "Microswimmers in an axisymmetric vortex flow," New J. Phys. **22**, 053051 (2020).
[28]I. Tanasijevic and E. Lauga, "Microswimmers in vortices: Dynamics and trapping," Soft Matter **18**, 8931–8944 (2022).
[29]S. A. Berman, J. Buggeln, D. A. Brantley, K. A. Mitchell, and T. H. Solomon, "Transport barriers to self-propelled particles in fluid flows," Phys. Rev. Fluids **6**, L012501 (2021).
[30]H. Yoest, J. Buggeln, M. Doan, P. Johnson, S. A. Berman, K. A. Mitchell, and T. H. Solomon, "Barriers impeding active mixing of swimming microbes in a hyperbolic flow," Front. Phys. **10**, 861616 (2022).
[31]N. Le, C. M. Miller, J. S. Detrick, C. R. Lodi, K. A. Mitchell, and T. H. Solomon, "Barriers and chutes for mixing of active particles in a vortex chain flow," Phys. Rev. Fluids **9**, 054501 (2024).
[32]T. V. Kasyap, D. L. Koch, and M. Wu, "Hydrodynamic tracer diffusion in suspensions of swimming bacteria," Phys. Fluids **26**, 081901 (2014).
[33]R. S. MacKay, J. D. Meiss, and I. C. Percival, "Transport in Hamiltonian systems," Physica D **13**, 55 (1984).
[34]T. H. Solomon and J. P. Gollub, "Chaotic particle transport in time-dependent Rayleigh-Bénard convection," Phys. Rev. A **38**, 6280 (1988).
[35]J. M. Ottino, *The Kinematics of Mixing: Stretching, Chaos and Transport* (Cambridge University Press, Cambridge, 1989).
[36]V. Rom-Kedar, "Homoclinic tangles—Classification and applications," Nonlinearity **7**, 441 (1994).
[37]S. A. Berman and K. A. Mitchell, "Trapping of swimmers in a vortex lattice," Chaos **30**, 063121 (2020).
[38]N. Khurana, J. Blawzdziewicz, and N. T. Ouellette, "Reduced transport of self-propelled particles in fluid flows," Phys. Rev. Lett. **106**, 198104 (2011).
[39]B. Qin and P. E. Arratia, "Confinement, chaotic transport, and trapping of active swimmers in time-periodic flows," Sci. Adv. **8**, eadd6196 (2022).
[40]G. M. Zaslavsky, "Dynamical traps," Physica D **168–169**, 292–304 (2002).
[41]M. F. Shlesinger, G. M. Zaslavsky, and J. Klafter, "Strange kinetics," Nature **363**, 31 (1993).
[42]T. H. Solomon, E. R. Weeks, and H. L. Swinney, "Observation of anomalous diffusion and Lévy flights in a two-dimensional rotating flow," Phys. Rev. Lett. **71**, 3975–3978 (1993).
[43]E. R. Weeks, J. S. Urbach, and H. L. Swinney, "Anomalous diffusion in asymmetric random walks with a quasi-geostrophic flow example," Physica D **97**, 291–310 (1996).
[44]H. Aref, "Stirring by chaotic advection," J. Fluid Mech. **143**, 1 (1984).
[45]E. Ott, *Chaos in Dynamical Systems* (Cambridge University Press, Cambridge, 2002).
[46]T. H. Solomon, S. Tomas, and J. L. Warner, "The role of lobes in chaotic mixing of miscible and immiscible impurities," Phys. Rev. Lett. **77**, 2682 (1996).

[47]T. Dombre, U. Frisch, J. M. Greene, M. Hénon, A. Mehr, and A. M. Soward, "Chaotic streamlines in the ABC flows," J. Fluid Mech. **167**, 353–391 (1986).
[48]M. A. Fogleman, M. J. Fawcett, and T. H. Solomon, "Lagrangian chaos and correlated Lévy flights in a non-Beltrami flow," Phys. Rev. E **63**, 020101(R) (2001).
[49]T. Solomon, E. R. Weeks, and H. L. Swinney, "Chaotic advection in a two-dimensional flow: Lévy flights and anomalous diffusion," Physica D **76**, 70–84 (1994).
[50]H. Willaime, O. Cardoso, and P. Tabeling, "Spatiotemporal intermittency in lines of vortices," Phys. Rev. E **48**, 288 (1993).
[51]J. M. Widholm, "The use of fluorescein diacetate and phenosafranine for determining viability of cultured plant cells," Stain Technol. **47**, 189 (1972).
[52]M. Onji, T. Sawabe, and Y. Ezura, "An evaluation of viable staining dyes suitable for marine phytoplankton," Bull. Fac. Fish. Hokkaido Univ. **51**, 153 (2000).
[53]T. Whitney, T. H. Solomon, and K. A. Mitchell "General approach to the statistics of microbial orientation: Levy walks, noise, and deterministic motion," Phys. Rev. E. (submitted).
[54]J. C. Crocker and E. R. Weeks, "Particle tracking using IDL," see http://physics.emory.edu/faculty/weeks/idl/ (2011).
[55]S. Chandresekhar, *Hydrodynamic and Hydromagnetic Stability* (Clarendon, Oxford, 1961).
[56]J. B. Dingwell, "Lyapunov exponents," in *Wiley Encyclopedia of Biomedical Engineering* (John Wiley & Sons, 2006).
[57]R. E. Goldstein, "Green algae as model organisms for biological fluid dynamics," Annu. Rev. Fluid Mech. **47**, 343–375 (2015).
[58]H. Chen and J.-L. Thiffeault, "Shape matters: A Brownian microswimmer in a channel," J. Fluid Mech. **916**, A15 (2021).
[59]D. H. Kelley and N. T. Ouellette, "Separating stretching from folding in fluid mixing," Nat. Phys. **7**, 477–480 (2011).
[60]J. Klafter, A. Blumen, and M. F. Shlesinger, "Stochastic pathway to anomalous diffusion," Phys. Rev. A **35**, 3081 (1987).
[61]E. R. Weeks and H. L. Swinney, "Anomalous diffusion resulting from strongly asymmetric random walks," Phys. Rev. E **57**, 4915–4920 (1998).